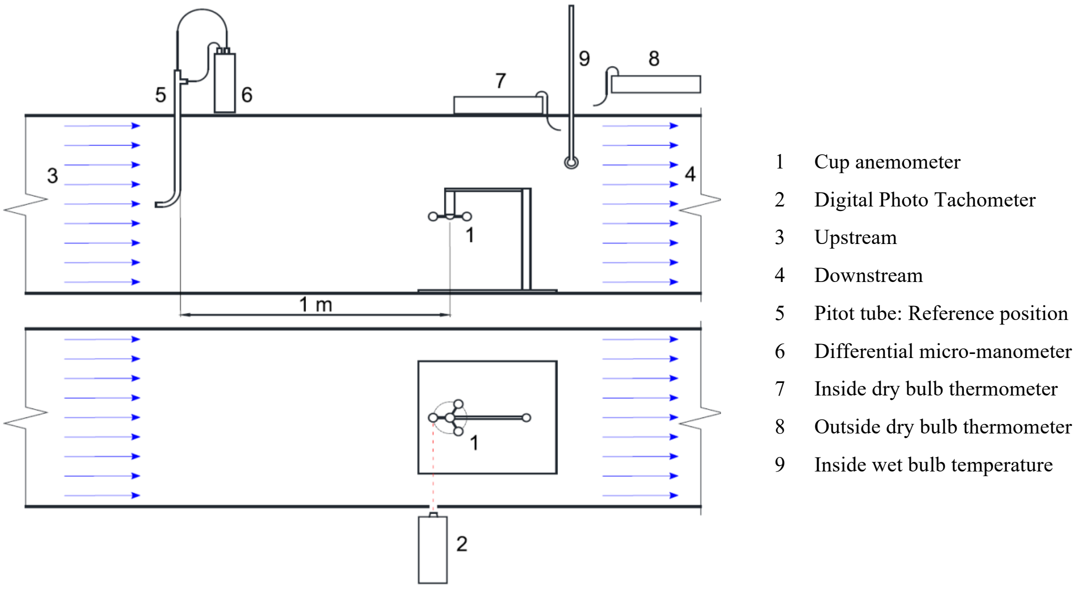

Fig. 3. Experimental setup. Up: front view, down: top view.

During the tests, the dry bulb temperature inside the tunnel varied between 22.3 ºC and 26.6 ºC; the tunnel wet bulb temperature between 16 ºC and 22 ºC; and the laboratory barometric pressure between 1012.81 hPa and 1023.84 hPa. These changes in the variables correspond to the natural environmental changes recorded during five days of testing. Once the barometric pressure, dry and wet bulb temperature are measured for each operating condition, the relative humidity $\emptyset$ can be determined by means of the Ferrel equation [13]:

$$\emptyset = \frac{P_{vs}(T_v) - \varphi \cdot P_B \cdot (T - T_v)}{P_{vs}(T)} = \frac{P_{vs}(T_v) - \varphi_0 \cdot (1 + 0.00115 \cdot (T_v - 273.15)) \cdot P_B \cdot (T - T_v)}{P_{vs}(T)}, \quad (2)$$

where T_v is the absolute wet bulb temperature (K), φ is the so-called psychometric constant pertinent to the standard wet-bulb temperature, φ_0 is the so-called psychometric constant pertinent to the standard wet-bulb temperature of 0 °C, which was experimentally adjusted by Ferrel. Table 1 provides the values of the coefficients in Eqs. (2)-(4), (6)-(7), P_B is the barometric pressure, and T is the absolute temperature (K). Eq. (3) is used to obtain the saturated vapor pressure, P_{vs}:

$$P_{vs}(T) = 1Pa \cdot e^{\left(\hat{A} \cdot T^2 + \hat{B} \cdot T + \hat{C} + \hat{D}/_T\right)}. \quad (3)$$

Once the relative humidity is known, the moist air density for each operating condition can be obtained via the CIPM-2007 revised formula [14], which is valid for the temperature and barometric pressure ranges of this work:

$$\rho = \frac{P_B \cdot M_a}{Z \cdot R \cdot T} \cdot \left[1 - x_v\left(1 - \frac{M_v}{M_a}\right)\right], \quad (4)$$

R is the ideal gas constant, M_a is the molar mass of dry air and M_v is the molar mass of water. The following equations are used to determine: the mole fraction of water vapour x_v, the enhancement factor f and the compressibility factor Z:

$$x_v = \emptyset \cdot f(P_B, t) \cdot \frac{P_v(T)}{P_B}, \quad (5)$$

$$f = \alpha + \beta \cdot P_B + \gamma \cdot t^2, \quad (6)$$

$$Z = 1 - \frac{P_B}{T} \cdot [a_0 + a_1 \cdot t + a_2 \cdot t^2 + (b_0 + b_1 \cdot t) \cdot x_v + (c_0 + c_1 \cdot t) \cdot x_v^2] + \frac{P_B^2}{T^2} \cdot (d + e \cdot x_v^2), \quad (7)$$

where t is the air-dry bulb temperature expressed in ºC and P_v is the partial vapor pressure (Pa).

In Section 3, a dimensional analysis based on the Reynolds number is performed. Thus, the determination of the moist air dynamic viscosity μ is required. This property can be calculated via the theoretical formulation of Mason & Monchick [15],which was experimentally validated by Kestin & Whitelaw [16] by means of an oscillating disc viscometer, and it is recommended by "NASA Langley Research Centre" [17] for outdoor-indoor air applications considering atmospheric pressure, a temperature between 10 ºC and 50 ºC, and a relative humidity in the range from 0.3% to 92%:

$$\mu = \alpha_0 + \alpha_1 \cdot T + (\alpha_2 + \alpha_3 \cdot T) \cdot x_v + \alpha_4 \cdot T^2 + \alpha_5 \cdot x_v^2, \quad (8)$$

According to the obtained results, the relative humidity during the tests was always within the interval 37.4%-66.8%; the moist air density within the interval 1.1738 kg/m^3 - 1.1982 kg/m^3, which means an air density variation equal to 2.44 g/m^3; and the dynamic viscosity remained almost constant since the measures were within the interval from $1.82 \cdot 10^{-5}$ Pa·s to $1.84 \cdot 10^{-5}$ Pa·s.

The anemometer rotation frequency, for each tested wind speed, is recorded with a sampling frequency of 1 Hz during 50 s, so that steady-state conditions can be considered. The cup anemometer rotation frequency f_r is calculated as the mean value of the m measurements recorded:

$$f_r = \frac{1}{m} \sum_{j=1}^{m} f_{rj}. \quad (11)$$

Table 1.- Constant coefficients for the determination of environmental properties.

Constant terms			Value	Units	Notes
Ferrel Eq. (2)		α_0	6.6·10^{-4}	ºC^{-1}	Adjusted by Ferrel
Vapour pressure Eq. (3)		$\hat{A}$	1.2378847·10^{-5}	K^{-2}	Specified by P. Giacomo [18]
		$\hat{B}$	-1.9121316·10^{-2}	K^{-1}	
		$\hat{C}$	33.93711047		
		$\hat{D}$	-6.3431645·10^{3}	K	
Moist air density Eq. (4)	*Ideal gas constant*	R	8.314472	J·mol^{-1}·K^{-1}	Recommended by Codata 2006 [19]
	Molar mass of dry air	M_a	28.96546·10^{-3}	kg·mol^{-1}	It is assumed a background of 400 µmol·mol^{-1} for the mole fraction of carbon dioxide in air
	Molar mass of water	M_v	18.01528·10^{-3}	kg·mol^{-1}	
Enhancement factor Eq. (6)		α	1.00062		Specified by P. Giacomo [18]
		β	3.14·10^{-8}	Pa^{-1}	
		γ	5.6·10^{-7}	K^{-2}	
The compressibility factor Eq. (7)		a_0	1.58123·10^{-6}	K·Pa^{-1}	Specified by P. Giacomo [18]
		a_1	-2.9331·10^{-8}	Pa^{-1}	
		a_2	1.1043·10^{-10}	K^{-1}·Pa^{-1}	
		b_0	5.707·10^{-6}	K·Pa^{-1}	
		b_1	-2.051·10^{-8}	Pa^{-1}	
		c_0	1.9898·10^{-4}	K·Pa^{-1}	
		c_1	-2.376·10^{-6}	Pa^{-1}	
		d	1.83·10^{-11}	K^{2}·Pa^{-2}	
		e	-0.765·10^{-8}	K^{2}·Pa^{-2}	
The dynamic viscosity Eq. (8)		α_0	8.4986·10^{-7}	Pa·s	Determined by Mason & Monchick. Recommended by NASA [17]
		α_1	7·10^{-8}	Pa·s·K^{-1}	
		α_2	1.13157·10^{-6}	Pa·s	
		α_3	-1·10^{-8}	Pa·s·K^{-1}	
		α_4	-3.7501·10^{-11}	Pa·s·K^{-2}	
		α_5	-1.00015·10^{-6}	Pa·s	

In the middle of the rotation frequency sampling interval, the dynamic pressure is recorded by means of the Pitot tube, which provides the mean value of $l = 20$ measurements obtained during 10 s previous to trigger it. The mean wind dynamic pressure Δp at the anemometer position for each operating condition is corrected through several factors detailed below:

$$\Delta p = \frac{k_\mathrm{c}}{C_\mathrm{h}} \cdot k_\mathrm{f}^2 \cdot \frac{1}{l} \sum_{k=1}^{l} \Delta p_i . \qquad (9)$$

The comparison between measurements from the Pitot tube placed at the reference position and at the anemometer position (Fig. 3) allows obtaining the wind tunnel calibration factor k_c and its uncertainty. The alignment accuracy of the Pitot tube with the wind flow direction is determined via the Pitot tube head coefficient C_h. In the present study, the value of this coefficient is determined according to the recommendations given by the ISO 3966, which deals with measurement of fluid flow velocity using Pitot static tubes [20]. Finally, the influence of the anemometer shape on the mean flow field velocity V_b is quantified by the blockage correction factor k_f calculated by applying the Maskell theorem [21]:

$$k_f = \frac{V_\mathrm{b}}{V} = 1 + \frac{1}{2} a \cdot c_\mathrm{f} \cdot b, \qquad (12)$$

where b, the blockage ratio, is the ratio of front area to the tunnel cross section; in our case b = 0.025. According to the recommendations of Barlow et al. [22], regarding unusual shapes tested in a wind tunnel, the product of the shape factor a and the force coefficient c_f is 0.5. The value of k_f is experimentally checked in our wind tunnel by comparing the measurements provided by the Pitot tube placed at the anemometer section with and without the cup anemometer inside the tunnel.

Finally, Eq. (10), which is obtained from Bernoulli's equation, provides the wind speed V at the anemometer location:

$$V = \sqrt{\frac{2 \cdot \Delta p}{\rho}}, \qquad (10)$$

The uncertainties of the different magnitudes are obtained following the Guide to the Expression of Uncertainty, commonly referred to as GUM [23]; besides that, the methodology employed by CENAM [24] is useful to determine the uncertainty of the moist air density and viscosity.

3. Results and discussion

3.1. Direct measurements and dimensionless abacus

Fig. 4 shows the f_r and V measures accomplished in the wind tunnel. It is remarkable the variations observed in f_r for a specific V, this means a low repeatability due to ambient conditions variability. Wind speed increases those variations from indistinguishable differences at low V=1.6 m/s to a 15 rad/s difference for V=17 m/s.

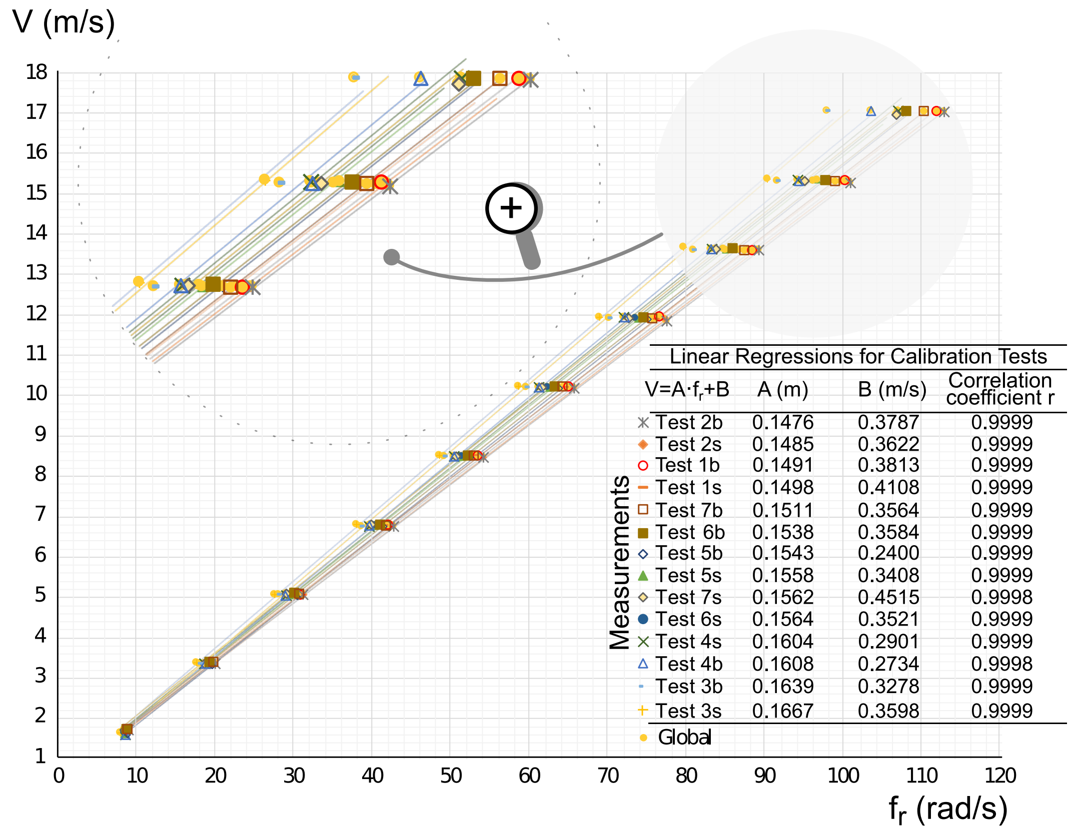

Fig. 4. Fourteen calibrations performed on the same cup anemometer at different ambient conditions.

In order to explain the discrepancies observed in the slope of the calibration lines in Fig. 4, the mean moist air density is calculated for each experimental test (Tests 1s-7s and Tests 1b-7b). The slope coefficients A are represented in Fig. 5 respect to their corresponding densities ρ. The large dispersion observed in each point (ρ, A), considering 95% confidence level, demonstrates that is difficult to fit ρ and A values by a linear regression, hereinafter referred to as "direct method".

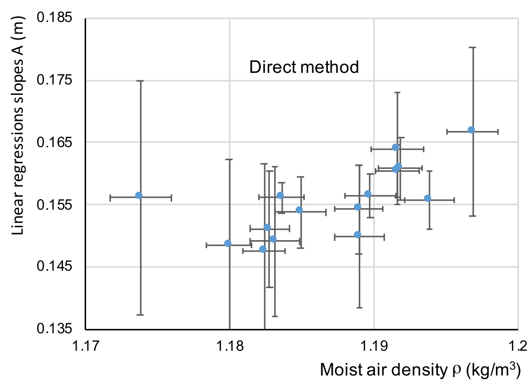

Fig. 5. Moist air density versus anemometer calibration slope: Direct Method. Bars represent a 95% confidence level.

In order to overcome the large uncertainties showed in Fig. 5, a dimensional analysis is conducted (Fig. 6). Applying the Buckingham Pi Theorem, the f_r - V domain is mapped into a new domain Π_1 - Π_2:

$$\Pi_1 = Re(f_r) = \frac{\rho \cdot f_r \cdot D^2}{\mu}, \qquad (11)$$

$$\Pi_2 = TSR^{-1} = \frac{V}{f_r \cdot D}, \qquad (12)$$

Reynolds number Re measures the ratio of inertia forces to viscous forces in a flow [25], and the Tip Speed Ratio TSR is the relation between the cup velocity and the free stream air speed.

The resulting "dimensionless abacus" is presented in Fig. 6. In this domain, the regression lines correspond to each tested wind speed, while the set of hyperbolic curves describes the measurements evolution respect to the inverse of the kinematic viscosity. Regression and correlation coefficients, as well as the correspondence of the hyperbolic lines with the moist air density (considering the dynamic viscosity quasi-constant during the experimental tests) are included in Fig. 6. Note that, the relative uncertainties of $Re(f_r)$ have low values. On the other hand, small density changes (in the order of hundredths of a kg/m^3) can modify the cup anemometer rotation frequency.

Considering a linear relation $V=A{\cdot}f_r+B$, such as in the direct method, and the dimensionless abacus, it is possible to determine A value as a function of the inverse of the kinematic viscosity ν^{-1} and f_r. Once the regression lines are determined, these lines and the Eqs. (11)-(12) provide the rotation frequency $f_{r,i}$ and ν_i^{-1} for specific Reynolds Re_i and wind speed V_i:

$$\frac{1}{TSR_i} = {}^{Re_i}/_{a_i} + b_i\,, \qquad (13)$$

$$f_{r,i} = \frac{TSR_i}{D} \cdot V_i\,, \quad (14)$$

$$\nu_i^{-1} = {}^{\rho_i}/_{\mu} = \frac{Re_i}{f_{r,i} \cdot D^2}\,. \qquad (15)$$

Finally, the slope coefficient A_i corresponding to $f_{r,i}$, and therefore to ν_i^{-1} is:

$$A_i = \frac{V_i - B}{f_{r,i}}\,. \qquad (16)$$

The following assumptions have been considered: firstly, if air density remains nearly constant during a calibration test, kinematic viscosity remains constant as well, and consequently, it is possible to determine a constant value for A; and secondly, the intercept coefficient B does not depend on kinematic viscosity (all calibration lines in Fig. 4 seem to have a similar intercept). The dynamic viscosity μ remains quasi-constant in the present research and in many practical applications, so it is easy to compute ρ_i from ν_i^{-1}.

The dimensional analysis provides the ρ-A values portrayed in Fig. 7 and the following linear model that estimates A for a specific ρ:

$$A = c \cdot \rho - d. \qquad (17)$$

The observed low dispersions, at 95% confidence interval, explain the high determination coefficient R^2=0.995 for the linear regression (Eq. (17)) provided by the hereafter called Dimensionless Abacus Method, compared to other studies [1], which use a Direct Method. Fig. 7 also shows the relative uncertainties of the calibration slope, moist air density and kinematic viscosity.

Eq. (17) shows how calibration lines change with the variation of air density at the laboratory, so that if air density increases, the slope of the calibration line increases as well, and vice versa.

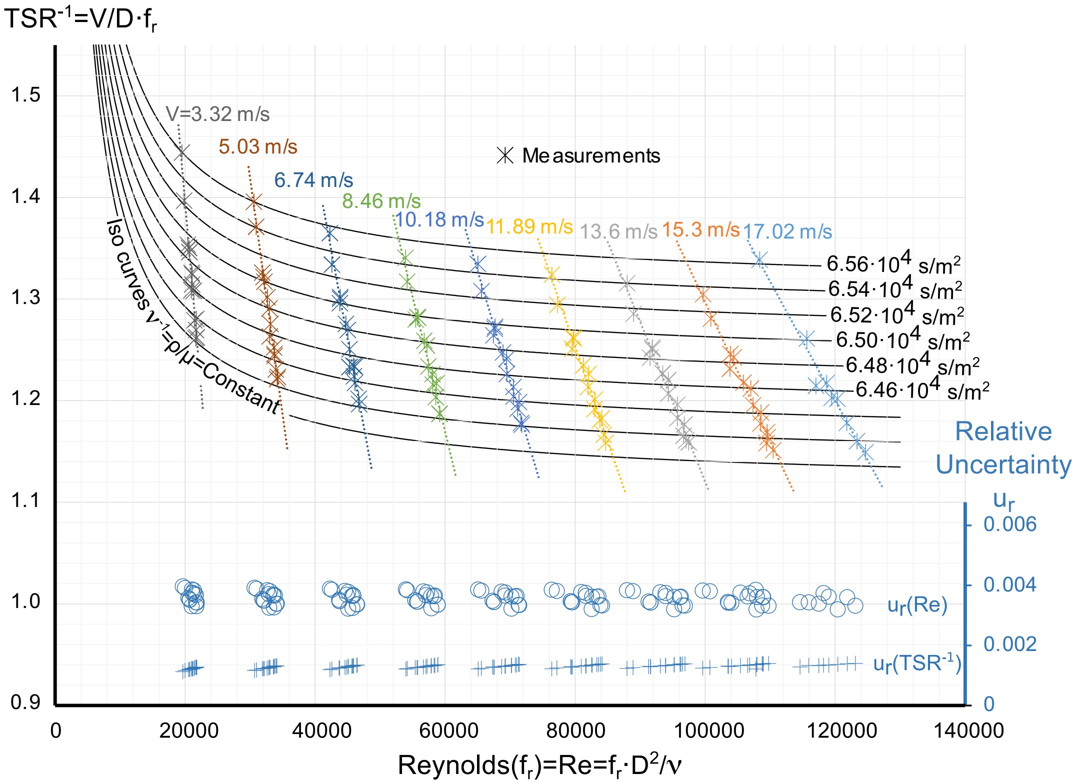

Fig. 6. Dimensionless abacus $Re(f_r) - TSR^{-1}$. Experimental values for several wind speeds at different ambient conditions (different air flow viscous forces).

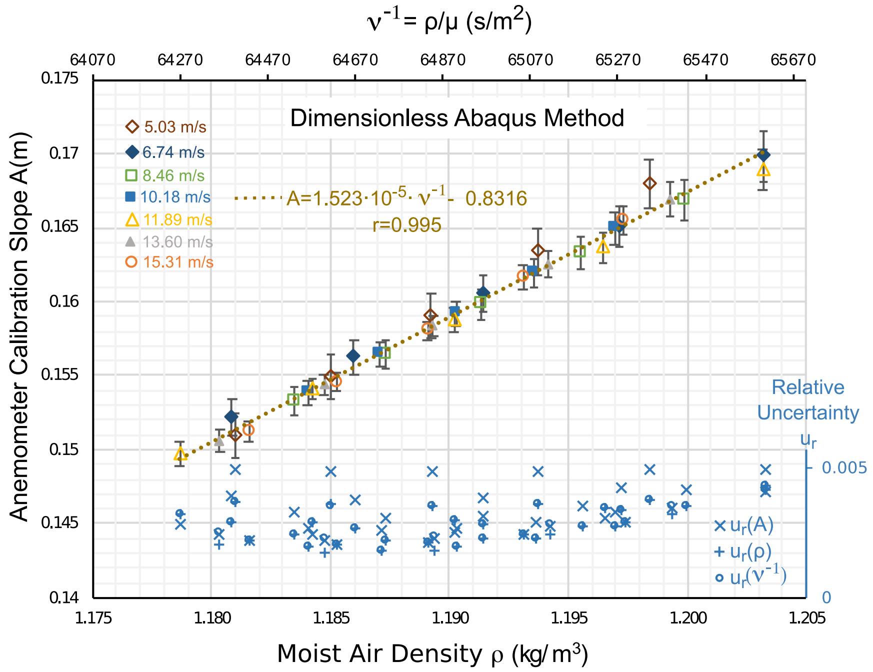

Fig. 7. Moist air density versus anemometer calibration line slope: Dimensionless abacus method. Bars represent a 95% confidence level.

Relative uncertainties are compared in Fig. 8.a. It is noteworthy the low and almost constant values provided by Dimensionless Abacus Method compared with Direct Method. Fig. 8.b classifies the relative uncertainties using the Dimensionless Abacus Method respect to wind speed. A reduction in relative uncertainty $u(A)/A$ is observed as the wind speed increases, this is a consequence of the manometer uncertainty, which growths as wind velocity decreases.

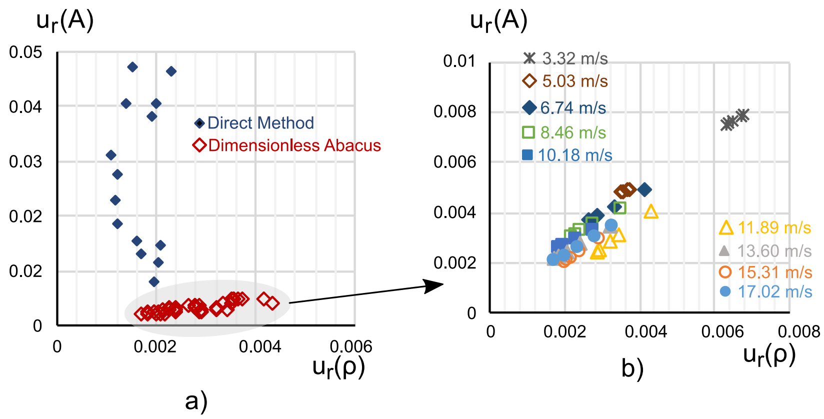

Fig. 8. Relative uncertainty of anemometer calibration line slope: a) Dimensionless Abacus Method versus Direct Method, b) Dimensionless Abacus Method values at tested wind speeds.

Note that, with the exception of V=3.32 m/s, the values represented in Fig. 7-8 lay within the wind speed range recommended by the annex F of the IEC international standard [11]. This range is stablished between 4 m/s and 16 m/s. According to the tests accomplished, the uncertainty is high for $V < 4$ m/s, and the linear Eq. (17) changes for $V > 16$ m/s.

3.2. The hyperbolic paraboloid surface.

The Eq. (17), obtained using the Dimensionless Abacus Method, helps to estimate A respect to ρ and therefore, the anemometer calibration Eq. (1) can be rewritten for $V \in$ [4 m/s, 15.3 m/s] as follows:

$$V = (c \cdot \rho - d) \cdot f_r + B\,, \qquad (18)$$

Eq. (18) is a hyperbolic-paraboloid surface: a doubly ruled surface, since it satisfies the conditions described for those quadratic surfaces [26]. According to Fig. 9, air density and rotation frequency isolines are the hyperbolic paraboloid surface rulings. In order to see the differences between the hyperbolic-paraboloid surface and the planar surface obtained by applying the IEC anemometry method [11], both surfaces have been extrapolated outside the measured density range (it is considered a mean density value during the calibration process equal to 1.1863 kg/m^3). When the anemometer is used in field application where the air density differs from that at the calibration laboratory, the measurement provided by the anemometer varies. The IEC method does not take into consideration this fact.

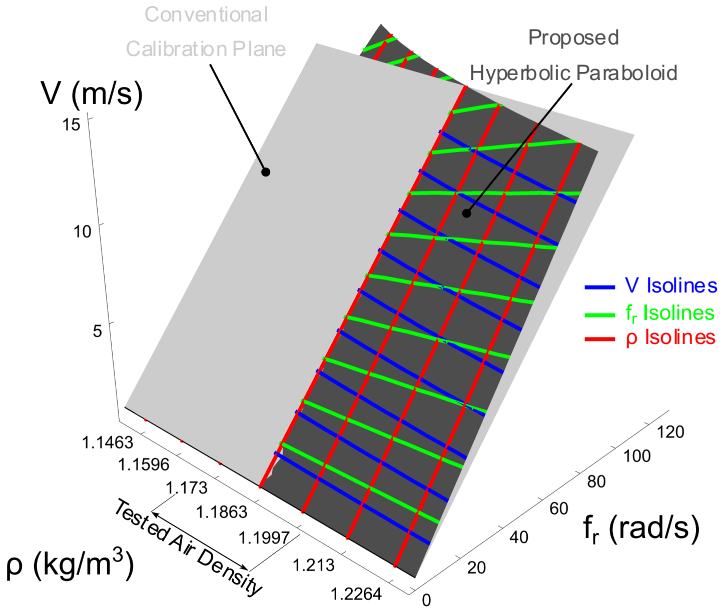

Fig. 9. Moist air density effect on an Auriol IAN cup anemometer. Calibration surfaces: Plane from the IEC anemometry method [11] and Hyperbolic Paraboloid from the Dimensionless Abacus Method.

Above $V = 15$ m/s the system does not behave as the ruled surface described by Eq. (18). A nonlinear response appears, which depends on the moist air density. It is noteworthy that, for air density measurements upper than 1.1863 kg/m^3, rotation frequency growths more slowly than if the air density is lower than 1.1863 kg/m^3.

Fig. 10 shows the ρ and f_r ruling lines as well as V isocurves (parabolas) in the $V(\rho, f_r)$ projected views. Note how the surface rulings evolve to curvilinear paths above 15 m/s (Fig. 10 a and b). Moreover, the curvature is concave for high moist air density values, and convex for low moist air density values. This effect of air density (or kinematic viscosity) could explains the underspeed or overspeed of cup anemometers observed in some field measurements, such as those highlighted by Kristensen [27,28], although this author relates this behaviour to the effect of air turbulence.

According to Fig. 10.b, the slope of the rotation frequency iso-curves, up to V=15 m/s, is a measure of how the wind speed changes ΔV due to air density variation $\Delta\rho$ during the IEC calibration process:

$$\frac{\Delta V}{\Delta \rho} = \mathrm{c} \cdot f_r^{*}, \qquad (19)$$

Eq. (19) depends on the anemometer and provides the slope of the rotation frequency iso-curves respect to: the cup anemometer rotation frequency considering the air density at the calibration laboratory f_r^*, and the "cup-anemometer air density sensibility" parameter c (Eq. (17)). For example, an Auriol IAN anemometer has a $c = 0.8315$ m^4/kg, if $f_r^* = 80$ rad/s, then a density variation of $\Delta\rho = 0.013$ kg/m^3 with respect to air density during the calibration process leads to $\Delta V = 0.86$ m/s, which will grow proportionally with the increments of air density.

Finally, Fig. 11 portrays the wind tunnel experimental data, the hyperboloid paraboloid surface and the IEC calibration line. The proposed Dimensionless Abacus model has a maximum absolute error of 0.4 m/s while the IEC calibration line has a maximum absolute error of 0.9 m/s.

In order to consider the influence of air density on wind speed measurements, the IEC linear regression [11] can be corrected by means of Eq. (19). On the other hand, the hyperboloid paraboloid surface considers the ambient conditions, thus wind speed estimation does not need additional corrections. In this regard, and according to Fig. 12, if $\rho > \rho_c$, where ρ_c is the air density at the calibration laboratory and ρ is the air density in a specific location, then the wind speed model obtained from the Direct Method provides values below the actual measurements, while if $\rho < \rho_c$ the Direct Method regression curve is above the real measurements. The hyperbolic parabolic regression does not need correction in any case.

The abacus showed in Fig. 6 and Eqs. (13), (15) point out that air-cup friction produces the aforementioned deviations. Hence, instead of air density, the kinematic viscosity is the most important ambient parameter. It is adequate the use of the moist air kinematic viscosity for wide ranges of temperature and density, such as those considered in Annex I of the IEC standard [11]: from 0.9 to 1.35 kg / m^3 (classifications A, B, C and D). For these cases, it is not possible to establish an equivalence between the air density and the inverse of the kinematic viscosity. Therefore, according to Fig. 7, Eqs. (17)-(19) should be rewritten respect to the inverse of the moist air kinematic viscosity as follows:

$$A = e \cdot {}^{1}/_{\nu} - d, \qquad (20)$$

$$V = \left(e \cdot {}^{1}/_{\nu} - \mathrm{d}\right) \cdot f_r + \mathrm{B}, \qquad (21)$$

$$\frac{\Delta V}{\Delta(1/\nu)} = e \cdot f_v^{*}, \qquad (22)$$

the parameter e is the "cup-anemometer air kinematic viscosity sensibility", and f_v^* is the equivalent rotation frequency when in-field air kinematic viscosity is equal to that of the calibration laboratory.

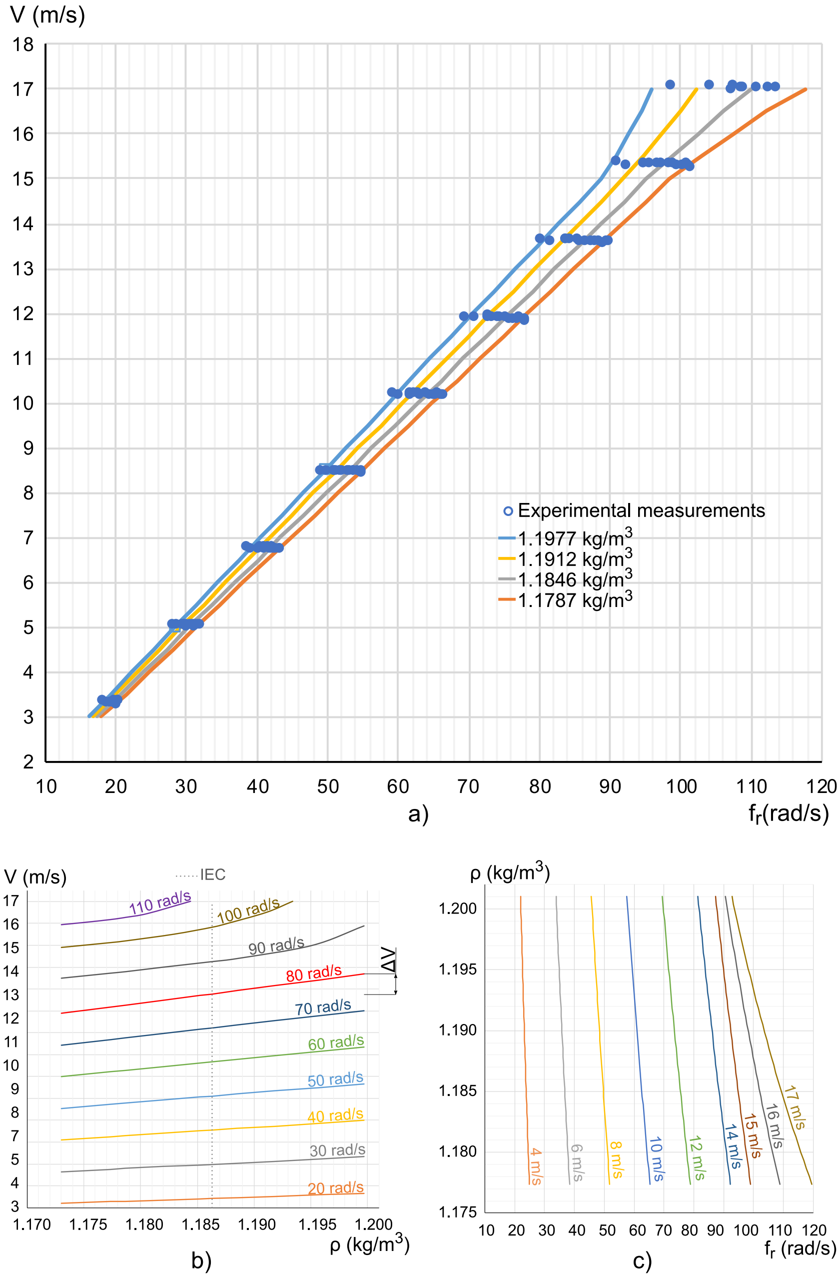

Fig. 10. Projected views of the Auriol IAN calibration surface. a) Front view, b) Top view, c) Side view.

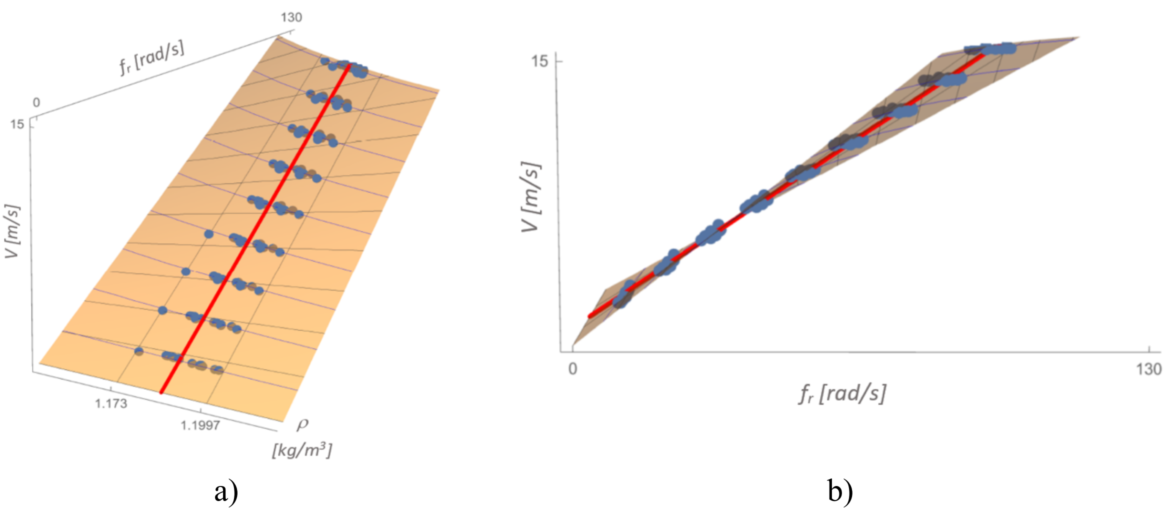

Fig. 11. Two views of the experimental observations fitting: the surface is the hyperbolic paraboloid that take into account ambient conditions, and the highlighted line is obtained from the IEC anemometry method [11].

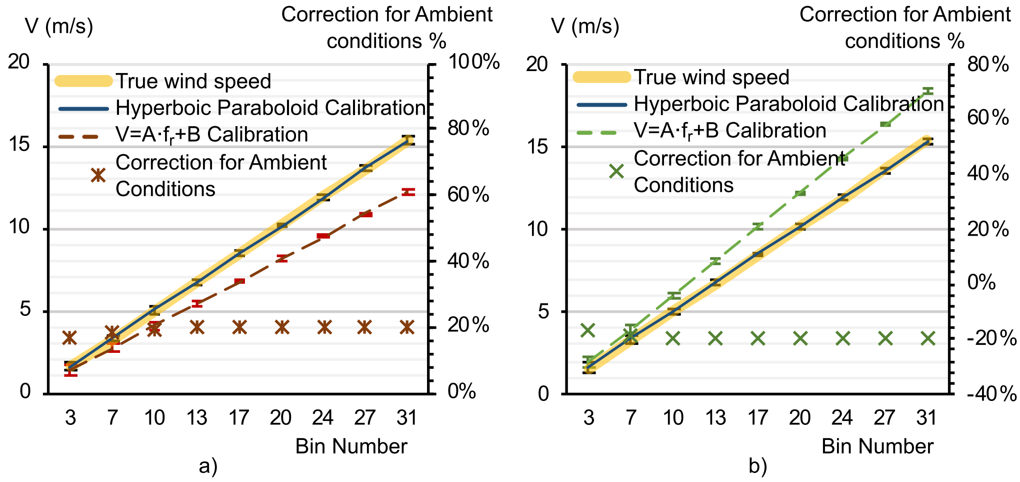

Fig. 12. Example of Direct Method and Dimensionless Abacus Method regressions models for an Auriol IAN cup anemometer. a) $\rho_c = 1.1863$ kg/m^3, $\rho = 1.225$ kg/m^3, b) $\rho_c = 1.1863$ kg/m^3, $\rho = 1.1476$ kg/m^3.

3.3. Annual Energy Production.

Annual Energy Production AEP, which depends on the turbine power curve and the wind speed probability distribution during a year, is key to study turbines performance.

The power curve relates wind speed and output power. According to the bin method described in the IEC 61400-12-1 international standard [1], an average value of wind speed and power corresponds to a specific bin (wind speed V_i- electrical power P_i) of the power curve. This method does not consider the influence of density variations between field and calibration laboratory on power curves.

A study case is presented to understand the role of the aforementioned density variations in power curves definition. In this case, the power data and wind speed measures provided in page 67 of the IEC 61400-12-1 standard [1] are used considering that wind speed was obtained by means of the analysed Auriol anemometer. Fig. 13 shows the resulting power curves. If the in-field air density ρ is greater than that at the calibration laboratory ρ_c, then the corrected power curve is beneath the power curve provided by the bin method (Fig. 13.a) and, on the contrary, when $\rho_c > \rho$ the bin method curve is beneath the corrected power curve (Fig. 13.b). Note that, even small density variations (±0.04 kg/m^3 in Fig. 13) lead to significant differences on the power curves (up to 20% of relative error, see Fig. 13). Actually, kinematic viscosity is the responsible of the cup anemometer rotation speed variations and therefore, it should be the parameter for correcting the power curve. Nevertheless, as it was previously discussed, for small density variations there is a direct relationship between density and the inverse of the kinematic viscosity so that density can be used instead of viscosity to correct the power curve.

According to the observed results in Fig. 13, power curves should be corrected in order to compare the turbine performance at different locations with different densities. This correction involves applying Eq. 19, which depends on the anemometer used; for the studied Auriol anemometer the value of *c* coefficient is shown in Fig. 7.

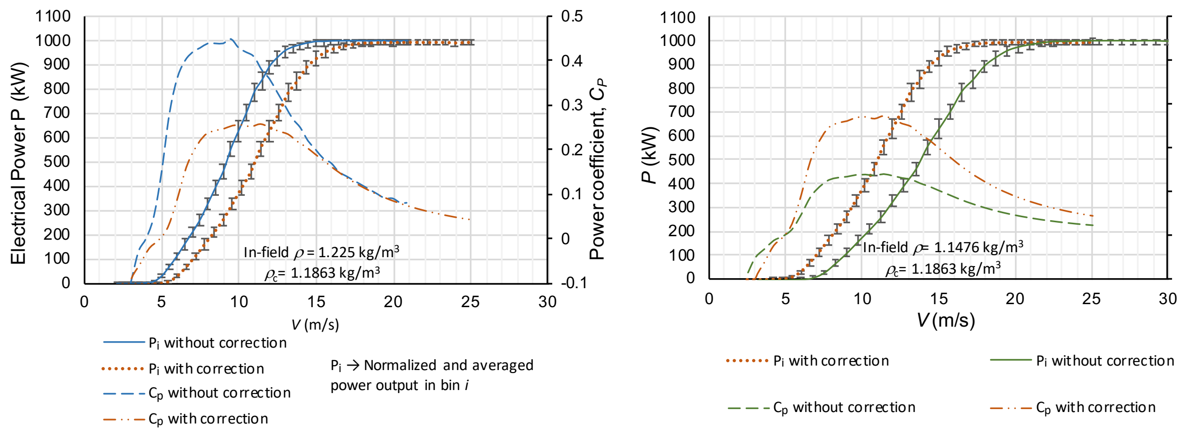

Fig. 13. Study case: power curves and power coefficient C_P curves. a) $\rho > \rho_c$ b) $\rho_c > \rho$. Confidence intervals with a coverage factor of one.

In addition to the power curve, it is necessary a wind speed probability distribution for AEP estimation. This probability distribution is also affected by the ambient conditions. The same method previously discussed can be applied to correct this distribution considering the density of a specific place and the used cup anemometer.

For the study case under consideration, Fig. 14 shows the resulting wind speed Weibull cumulative distribution $F(V_i)$ and its probability distribution with and without density corrections at two locations with different air densities. For a place with $\rho > \rho_c$, the viscous effects slow down the anemometer's rotational speed respect to the rotation speed observed during calibration. This means that the frequency assigned to a wind speed without density correction should be assigned to a higher wind speed. On the contrary, in locations with lower density, the viscous effects are reduced, which increases the anemometer's rotational speed and therefore, the wind speed value provided by the anemometer is higher than the actual one. Fig. 14 also portrays the wind speed frequencies with and without correction. The mode values of the wind speed frequency curves comply with the abovementioned observations: higher mode value for the corrected curve at places with air density greater than the calibration one (Fig. 14.a) and vice versa. Recall that in this study case there are small density variations, otherwise viscosity should be considered instead of density.

It is worth to note that it is impossible to make rigorous comparisons between wind frequency curves of two different sites without accomplishing corrections for ambient conditions. The average annual wind speed (or the Weibull scale factor) should be corrected upwards at those places with air density above the calibration one (typically coastal locations), and otherwise it should be corrected downwards (typically interior or mountainous locations).

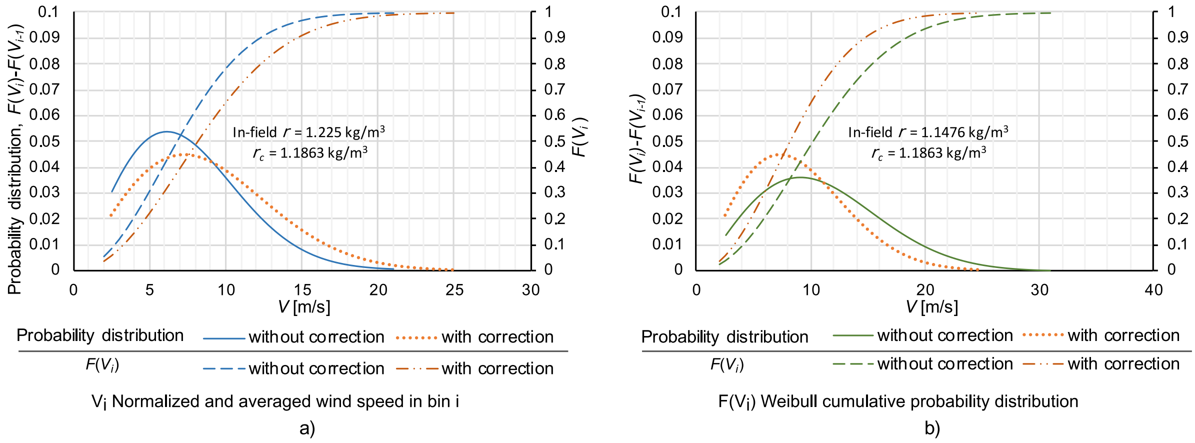

Fig. 14. Study case: Weibull cumulative probability distribution and wind speed frequency distribution: a) $\rho > \rho_c$ b) $\rho_c > \rho$

Finally, according to the international standard IEC 61400-12-1 [1], specific AEP is calculated as the product of power curve and the wind speed frequency distribution at a specific site, while generic AEP is obtained by multiplying measured power curve by a set of reference distributions for wind speed frequency. Each reference distribution has a mean value of wind speed measured at hub height. Fig. 15 shows specific and generic AEP measured using the power curves and the frequency distributions shown in Figs. 13-14. Generic AEP is typically used for design optimization of wind turbines [29] and specific AEP is used for determining the optimal location among several proposed places for the installation of a wind turbine [30].

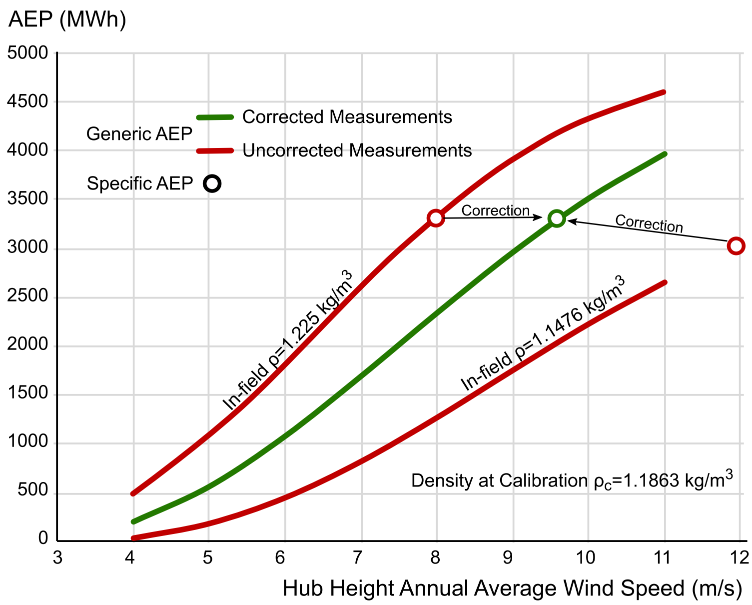

Fig. 15. Example of specific and generic AEP using an Auriol IAN cup anemometer, ρ_c= 1.1863 kg/m^3.

Regarding generic AEP, it is observed that the values at sites with $\rho > \rho_c$ should be corrected downward; whereas when the generic AEP is calculated in locations with $\rho < \rho_c$, the generic AEP should be corrected upwards. Therefore, when calculating estimations of generic AEP, the effect of the variation in ambient conditions between the measuring location and the calibration laboratory of the anemometer must be considered. The effect of air density can be corrected by means of Eq. (19). Nevertheless, if the variation range of density is significant, the correction should be based on the kinematic viscosity, as it is stated in Eq. (22).

As explained above, the specific AEP for a particular location can be calculated from the mean power curve and the wind speed specific frequency curve. If both curves are measured at the same time and using the same anemometer, the resulting value of the specific AEP does not require a correction of the effect of air density during the calibration procedure (see Fig. 15). This is because the correction affects both curves in an inversely proportional way, which leads the result of the multiplication to remain unaffected. The problem arises from the fact that is necessary to measure the wind turbine power curve at its final location, or at a near one. Nevertheless, the research literature shows that the same anemometer is rarely used, due to the manufacturer power curve is used [30] or wind speeds are obtained from wind resource maps [31,32].

The proposed correction procedure allows to study the wind energy potential of a wind turbine before installing it in a specific location. The idea is to correct a known power curve of the wind turbine considering the variation of air density between a specific place where the turbine could be installed and the calibration laboratory.

4. Conclusions

This work provides an explanation for those cases where a cup-anemometer has different rotation frequencies for the same wind speed. According to a set of experimental measurements conducted in a wind tunnel, we concluded that the main cause of the abovementioned variations are the kinematic viscosity variations or, equivalently, the density variations when a constant dynamic viscosity can be assumed. Moreover, we verified that the experimental observations fit adequately to a hyperbolic paraboloid surface, which relates wind speed, rotation frequency and density.

The proposed relation leads to more accurate wind speed measurements. Hence, it helps to improve the AEP estimations by reducing the error linked to the cup-anemometers calibration procedure. On the other hand, in view of the presented results, for those that prefer a conventional calibration (which is accomplished considering a constant density), we described a procedure to correct in-field wind speed measurements according the specific density conditions.

Respect to the observations that foster this work, even for a low-density variation of 0.0267 kg/m^3, we noted differences up to 20 rd/s for a constant wind speed of 17 m/s as we showed in Figure 4. A linear regression between the slopes A of V-f_r calibration curves for different densities failed due to great dispersion of (ρ, A) data (Figure 5).

In order to overcome the above drawback, we discovered that representing the information in a TSR^{-1} vs Re diagram, it is possible to estimate the calibration slope coefficient with a relative uncertainty lower than 0.005, as a linear function of the density or the kinematic viscosity. The resulting relation among wind speed, rotation frequency and density is a type of ruled surface (a hyperbolic paraboloid surface). This surface, fitted using our experimental data, has a maximum absolute error of 0.4 m/s while the conventional calibration line has a maximum absolute error of 0.9 m/s. Experimental results show that, when field air density varies ±0.01 kg/m^3 from that at the calibration laboratory, the error in wind speed provided by the cup anemometer is about ±5%. The conventional calibration can be improved by correcting the measure with $\pm\Delta V$ that depends on the air density and the coefficient c (cup-anemometer air density sensibility) of the hyperbolic paraboloid surface (Eq. 19).

Regarding wind turbine power curves, if in-field measurements of wind speed with a cup-anemometer are not corrected, a 50% variation in the power coefficient C_P is observed when the same wind turbine is tested at several locations whose air density slightly differs from that at the calibration laboratory. Therefore, wind power curves for the same turbine differs significantly depending on the location where the observations are made. If the correction procedure proposed in the present study is applied, the estimated value of wind turbine power decreases as in-field air density increases respect to that of the calibration laboratory, and vice versa. Therefore, the proposed procedure provides the same power curves for a particular cup-anemometer regardless of the location where measurements are performed.

Additionally, using the power data and wind speed measures provided by the IEC 61400-12-1 standard for a 1 MW wind turbine, we computed the AEP with and without applying the developed equation for cup anemometers. The results of this computation showed for example, overestimations of 1000 MWh/year for an annual mean wind speed of 10 m/s measured at hub height in a location where air density is about 0.04 kg/m^3 higher than that at the calibration laboratory, and underestimations about 1250 MWh/year when density is 0.04 kg/m^3 lower. The error of the estimation is even greater for lower wind speeds.

Just in case of determining the power curve and the wind speed specific frequency at the same location and with the same anemometer, specific AEP estimations don’t require anemometer correction. Therefore, this case is feasible only when measuring an existing wind turbine.

Finally, the following bullets summarize the main findings of this work:

- The rotation frequency variations for constant wind speeds in cup-anemometers are due to kinematic viscosity variations.
- A hyperbolic paraboloid surface that relates wind speed, rotation frequency and kinematic viscosity provides a more accurate wind speed estimation than a linear regression between wind speed and rotation frequency at constant density.
- The accuracy of cup anemometers would improve significantly by considering the calibration error and, consequently, wind speed measurements would lead to more accurate AEP estimations.”

The novelty and interest of the summarizing findings are that they quantitatively explain the observed rotation frequency variations in a cup anemometer respect to ambient conditions. The proposed approach would improve the reproducibility of the measurements provided by cup anemometers, which would increase the reliability of these devices when they are used to perform power curves, statistical studies regarding wind speed and estimations of AEP.

Since the proposed approach has been done using wind tunnel measurements and a specific anemometer, future works that would help to support the presented results could be to perform in field measurements with different anemometers, or do the cup-anemometer calibration in a wind tunnel that allows large variations in air density. For this last case, the wind tunnels must allow a regulation of air pressure, so that it can be slightly modified respect to the ambient pressure.

Acknowledgments
The authors would like to acknowledge the usage of the wind tunnel provided by the fluid mechanics area belonging to the department of Mechanical and Mining Engineering of the University of Jaén.

References

1. Pindado, S.; Sanz, A.; Wery, A. Deviation of cup and propeller anemometer calibration results with air density. *Energies* **2012**, *5*, 683-701.
2. Kristensen, L. Cup anemometer behavior in turbulent environments. *Journal of Atmospheric and Oceanic Technology* **1998**, *15*, 5-17.
3. Ligęza, P. An alternative mathematical model of vane anemometers based on the balance of power. *Flow Measurement and Instrumentation* **2017**, *54*, 210-215.
4. Díaz, S.; Carta, J.A.; Matías, J.M. Performance assessment of five MCP models proposed for the estimation of long-term wind turbine power outputs at a target site using three machine learning techniques. *Applied Energy* **2018**, *209*, 455-477.
5. Díaz, S.; Carta, J.A.; Matías, J.M. Comparison of several measure-correlate-predict models using support vector regression techniques to estimate wind power densities. A case study. *Energy Conversion and Management* **2017**, *140*, 334-354.
6. Ulazia, A.; Gonzalez-Rojí, S.J.; Ibarra-Berastegi, G.; Carreno-Madinabeitia, S.; Sáenz, J.; Nafarrate, A. Seasonal air density variations over the East of Scotland and the consequences for offshore wind energy. In Proceedings of the 7th International Conference on Renewable Energy Research and Applications (ICRERA); 2018 Oct 14-17; Paris, France, pp. 261-265. doi: 10.1109/ICRERA.2018.8566716.
7. St Martin, C.M.; Lundquist, J.K.; Clifton, A.; Poulos, G.S.; Schreck, S.J. Wind turbine power production and annual energy production depend on atmospheric stability and turbulence. *Wind Energy Science (Online)* **2016**, *1*.
8. Marraccini, M.; Bak-Kristensen, K.; Horn, A.; Fifield, E.; Hansen, S. Influence of small-scale turbulence on cup anemometer calibrations. In Proceedings of Journal of Physics: Conference Series; 2017, Vol. 926, No 1. DOI: 10.1088/1742-6596/926/1/012005
9. Jin, Y.; Ju, P.; Rehtanz, C.; Wu, F.; Pan, X. Equivalent modeling of wind energy conversion considering overall effect of pitch angle controllers in wind farm. *Applied Energy* **2018**, *222*, 485-496.
10. Sedaghat, A.; Hassanzadeh, A.; Jamali, J.; Mostafaeipour, A.; Chen, W.-H. Determination of rated wind speed for maximum annual energy production of variable speed wind turbines. *Applied Energy* **2017**, *205*, 781-789.
11. International Electrotechnical Commission (IEC) Wind turbines – part 12–1: power performance measurements of electricity producing wind turbines, E.I.S., IEC 61400-12-1, Geneva, Switzerland. Wind turbines – part 12–1: power performance measurements of electricity producing wind turbines. In *IEC 61400-12-1*, 2018.
12. Atmosphere & Solar Radiation Modeling Group (MATRAS). Meteorological Station Database. http://www.ujaen.es/dep/fisica/estacion/estacion3.htm. Available online: (accessed on 2 May 2019).
13. Wexler, A.; Standards, U.S.N.B.o. *Humidity and Moisture: Fundamentals and standards. A. Wexler and W.A. Wildhack, editors*; Reinhold Publishing Corporation: 1965.
14. Picard, A.; Davis, R.; Gläser, M.; Fujii, K. Revised formula for the density of moist air (CIPM-2007). *Metrologia* **2008**, *45*, 149.
15. Mason, E.; Monchick, L. Survey of the equation of state and transport properties of moist gases. *Humidity and Moisture: Fundamentals and Standards* **1965**, 257-272.
16. Kestin, J.; Whitelaw, J. The viscosity of dry and humid air. *International Journal of Heat and Mass Transfer* **1964**, *7*, 1245-1255.
17. Zuckerwar, A.J.; Meredith, R.W. Low-frequency absorption of sound in air. *The Journal of the Acoustical Society of America* **1985**, *78*, 946-955.
18. Giacomo, P. Equation for the determination of the density of moist air (1981). *Metrologia* **1982**, *18*, 33.
19. Mohr, P.J.; Taylor, B.N. CODATA recommended values of the fundamental physical constants: 2002. *Reviews of modern physics* **2005**, *77*, 1.
20. Standardization; ISO-3966: 2008. Measurement of fluid flow in closed conduits-Velocity area method using Pitot static tubes.
21. Hansen, O.; Hansen, S.; Kristensen, L. Wind tunnel calibration of cup anemometers. In Proceedings of the AWEA Wind Power Conference; Oct 2012, pp. 1-22.
22. Barlow, J.B.; Rae, W.H.; Pope, A. Low-speed wind tunnel testing. **1999**.
23. JCGM/WG1. Guide to the Expression of Uncertainty in Measurement. International Organization for Standardization: Geneva, (Switzerland), 2008.
24. Becerra, L.; Guardado, M. Assessment of uncertainty in the air density determination. CENAM: 2003.
25. Anderson Jr, J.D. *Fundamentals of aerodynamics*, 6th ed.; McGraw-Hill Education: New York, 2016.
26. Weissen, E. Quadratic Surface. Availabe online: http://mathworld.wolfram.com/QuadraticSurface.html (accessed on 2 May 2019).
27. Busch, N.E.; Kristensen, L. Cup anemometer overspeeding. *Journal of Applied Meteorology* **1976**, *15*, 1328-1332.
28. Kristensen, L. Can A Cup AnemometerUnderspeed'? *Boundary-Layer Meteorology* **2002**, *103*, 163-172.
29. Ashuri, T.; Zaaijer, M.B.; Martins, J.R.; Zhang, J. Multidisciplinary design optimization of large wind turbines—Technical, economic, and design challenges. *Energy conversion and management* **2016**, *123*, 56-70.
30. Aukitino, T.; Khan, M.; Ahmed, M.R. Wind energy resource assessment for Kiribati with a comparison of different methods of determining Weibull parameters. *Energy Conversion and Management* **2017**, *151*, 641-660.
31. Villena-Ruiz, R.; Ramirez, F.J.; Honrubia-Escribano, A.; Gomez-Lazaro, E. A techno-economic analysis of a real wind farm repowering experience: The Malpica case. *Energy Conversion and Management* **2018**, *172*, 182-199.
32. Jung, C.; Schindler, D.; Laible, J. National and global wind resource assessment under six wind turbine installation scenarios. *Energy Conversion and Management* **2018**, *156*, 403-415.